Terrestrial ecosystems enhanced root zone water storage capacity in response to climate change over the past four decades

Xi, Qiaojuan; Gao, Hongkai; Wang-Erlandsson, Lan; Dong, Jianzhi; Fenicia, Fabrizio; Savenije, Hubert H.G.; Hrachowitz, Markus

DOI
10.1016/j.scib.2025.06.027

Publication date
2025

Document Version
Final published version

Published in
Science Bulletin

Science Bulletin 70 (2025) 3019–3028

Contents lists available at ScienceDirect

Science Bulletin

journal homepage: www.elsevier.com/locate/scib

Article

Terrestrial ecosystems enhanced root zone water storage capacity in response to climate change over the past four decades

Qiaojuan Xi [a], Hongkai Gao [a,*], Lan Wang-Erlandsson [b,c,d], Jianzhi Dong [e], Fabrizio Fenicia [f], Hubert H.G. Savenije [g], Markus Hrachowitz [g]

[a] Key Laboratory of Geographic Information Science, Ministry of Education, School of Geographic Sciences, East China Normal University, Shanghai 200241, China
[b] Stockholm Resilience Centre (SRC), Stockholm University, Stockholm, 10691, Sweden
[c] Bolin Centre for Climate Research, Stockholm University, Stockholm, 10691, Sweden
[d] Potsdam Institute for Climate Impact Research (PIK), Member of the Leibniz Association, Potsdam, 14473, Germany
[e] Institute of Surface-Earth System Science, Tianjin University, Tianjin 300072, China
[f] Eawag, Swiss Federal Institute of Aquatic Science and Technology, Dubendorf, 8600, Switzerland
[g] Water Resources Section, Delft University of Technology, Delft, 2600, the Netherlands

ARTICLE INFO

Article history:
Received 29 December 2024
Received in revised form 9 June 2025
Accepted 10 June 2025
Available online 21 June 2025

Keywords:
Root zone water storage capacity
Mass curve technique
Climate change
Resilience
Trend analysis

ABSTRACT

Adaptation of ecosystems' root zones to climate change critically affects drought resilience and vegetation productivity. However, a global quantitative assessment of this mechanism is missing. In this study, we analyzed high-quality observation-based data to find that the global average root zone water storage capacity (S_R) increased by 11%, from 182 to 202 mm in 1982–2020. The total increase of S_R equals to 1652 billion m^3 over the past four decades. S_R increased in 9 out of 12 land cover types, while three relatively dry types experienced decreasing trends, potentially suggesting the crossing of ecosystems' tipping points. Our results underscore the importance of accounting for root zone dynamics under climate change to assess drought impacts.

1. Introduction

The root zone, underlying the land surface, cannot be directly observed at large scales with currently available observation technology. As such, it remains one of the most uncertain components of the global terrestrial ecosystem [1,2]. Climate change has intensified and extended meteorological droughts (i.e., precipitation deficits relative to atmospheric evaporation demand) [3,4], which are often associated with terrestrial ecosystem degradation, mortality, or even collapse [5,6]. Paradoxically, however, observations of vegetation greening indicate that, hitherto, increasing droughts have not resulted in an overall decline of global-scale vegetation [7,8]. Most studies attribute the increase in vegetation productivity to the CO_2 fertilization effect and land-use management [7,8]. Nevertheless, the role of belowground root zone adaptation to drought has largely been overlooked.

The root zone water storage capacity (S_R) of terrestrial ecosystems is a buffer to guarantee vegetation access to moisture during critical periods of drought [9,10]. For a given S_R, the vertical distribution of moisture may vary and its quantity does not necessarily correspond to the total volume of water in the unsaturated zone, but rather to the part of the soil moisture that is accessible to roots. For example, in the Loess Plateau of China where the unsaturated zone is thick, the root zone is limited to the active shallow layer of the topsoil [11]. On the other hand, in karst and rocky substrates, the root zone may encompass not only the soil water storage but also the fissure water storage in the bedrock [12]. In rainfall-runoff processes, S_R controls the partitioning of precipitation into drainage and evaporation. As such it is a key parameter not only in hydrological models but also in land-surface models, where it controls latent and sensible heat fluxes, as well as in ecohydrological models where it regulates vegetation dynamics [13,14]. It is well-documented that the accurate estimation of S_R significantly improves hydrological and land-surface model performance [13–15]. Large-sample data analysis revealed that ecosystems tend to optimize their root zones to allow for the most efficient extraction of water from the substrate, thereby meeting water demand (evaporation) while minimizing their carbon expenditure for root growth and maintenance [16–18]. S_R, as an integrated reflection

* Corresponding author.
E-mail address: hkgao@geo.ecnu.edu.cn (H. Gao).

https://doi.org/10.1016/j.scib.2025.06.027

of root density, distribution, depth, and lateral extension can serve as an effective proxy for belowground biomass.

Ecosystems' root zones are part of ecosystems' survival strategy and adaptive capacity and respond dynamically to changes in climatic and anthropogenic drivers [19]. Such changes in S_R, directly feed back to evaporation and biomass production, thus dynamically enhancing the water cycle as a whole [9,20]. Globally, S_R varies across climatic zones and landscapes, with larger S_R in areas with high seasonality, high aridity, longer dry periods, and larger rainfall variability (for example, tropical savanna and Mediterranean climate), and smaller S_R under relatively stable conditions (for example, tropical rainforests and temperate climates). Human activities, such as deforestation and irrigation, can also alter S_R. In experimental catchments in the USA and Germany, S_R was observed to sharply decline immediately after deforestation, and then gradually recover over 5–13 years [21]. Irrigation on agricultural land provides additional water during dry periods, artificially reducing the exposure of vegetation to droughts, leading to a smaller S_R than under natural conditions [10].

Although S_R is a key variable in runoff generation, drought resilience, and land-atmosphere interactions, a global quantitative assessment of the temporal evolution and spatial variation of S_R in response to climate change and anthropogenic activities is missing. Classical approaches to estimate S_R are based on combining information of soil texture and rooting depth from field observations using look-up tables by land-use categories, which are problematic to upscale. More importantly, being mostly snapshots in time, these approaches ignore the temporal dynamics of S_R [22]. Inverse model approaches based on satellite data of precipitation, evaporation, and other meteorological factors have previously been shown to be valuable in estimating rooting depths at large scales. However, such approaches require extensive parameterizations and assumptions on soil-plant-water relationships [16,23]. Some terrestrial biosphere models now use aboveground biomass changes as a surrogate of belowground responses [24]. However, the underlying assumption of a stationary plant biomass allocation remains to be tested.

In contrast to these methods, the mass curve technique (MCT), initially developed for determining reservoir capacity in civil engineering [25], allows for model- and scale-independent estimates of S_R. The MCT approach relies on the water balance and merely requires cumulative vertical inflow (rainfall, snowmelt, and irrigation) and outflow (dry spell evaporation) [9], which are all observable variables from *in-situ* measurements, reanalysis data, and satellite remote sensing [10]. Such time series of inflows and outflows are used to infer water deficit during dry spells, where the largest deficit over a sufficiently long period of time can be assumed to represent the actual S_R. The MCT approach has previously been used to estimate present-day S_R at both the catchment and global scale and has been shown to yield similar results as the inverse modelling approach and outcompete the look-up table approach [10,20]. Nevertheless, the MCT approach has yet to be used for quantifying global S_R dynamics in a changing environment.

In this study, we aim to quantify the spatial and temporal patterns of S_R, identify the drivers of observed change, and explore the contributions of S_R change to global greening. We applied the MCT approach to state-of-the-art high-quality reanalysis data to estimate S_R from 1982 to 2020 at the grid cell, regional, and global scales. Furthermore, we investigated the effect of drought duration and average daily water deficit on S_R trends. To explore the adaptation of global ecosystems to drought, we analyzed the relationship between belowground S_R and aboveground Leaf Area Index (LAI) changes in conjunction with variations in the aridity index (AI) at grid cell and regional scales.

2. Materials and methods

2.1. Data

To estimate S_R, we used the daily evaporation, precipitation, snowmelt, irrigation, and temperature data. The daily evaporation, precipitation, snowmelt, and temperature were obtained from the ERA5 reanalysis product, with a spatial resolution of 0.5°, covering the period 1971–2020. Irrigation data for 1971–2010 were derived from the ensemble average of four model outputs (WaterGAP, H80, LPJmL, and PCR-GLOBWB), adjusted by correction factors based on the difference between modelled estimates and reported records [26], with monthly temporal resolution and 0.5° spatial resolution. For the period 2011–2020, we assumed irrigation remained constant at 2010 levels. Monthly irrigation data were downscaled to daily resolution based on ERA5 daily evaporation. The input evaporation, precipitation, snowmelt, and irrigation data are shown in Fig. S1 (online).

The LAI and AI were used to explore the adaptation of ecosystems to drought, combined with S_R. This study employed three satellite-derived LAI products: GIMMS LAI4g, GLOBMAP LAI, and GLASS LAI. GIMMS LAI4g was constructed using spatiotemporally consistent BPNN models, the latest PKU GIMMS NDVI product, and high-quality global Landsat LAI samples to mitigate the effects of satellite orbital drift and sensor degradation [27]. It provided a half-month temporal resolution for the period 1982–2020, with a spatial resolution of 0.083°. To remove abnormal data in GIMMS LAI, values exceeding three times the maximum or falling below one-third of the minimum value of the three preceding and following temporal data points were excluded. Missing values in time series were subsequently filled using linear interpolation, and data were smoothed with Savitzky-Golay filtering with a window width of 7 and a smoothing polynomial of 3. GLOBMAP LAI was the fusion of MODIS and AVHRR with a half-month temporal resolution for 1982–2000 and an 8-day resolution for 2001–2020 with a spatial resolution of 0.073° [28]. GLASS LAI, which was generated using general regression neural networks (GRNNs), integrated satellite LAI time series and AVHRR surface reflectance data, providing an 8-day temporal resolution and a spatial resolution of 0.05° for 1982–2018 [29]. All three LAI datasets were resampled to a coarser resolution of 0.5°, and the annual average LAI for each dataset was calculated for further analysis.

The AI for the period 1982–2020 in this study was calculated through annual potential evaporation and precipitation using Eq. (1):

$$AI_n = \frac{PE_n}{P_n}, \tag{1}$$

where AI_n is the aridity index in year n, PE_n is the annual potential evaporation in year n, P_n is the annual precipitation in year n. The potential evaporation was obtained from Global Land Evaporation Amsterdam Model (GLEAM), available at a daily temporal resolution and 0.25° spatial resolution for the period 1982–2020. The data were resampled to 0.5° to match other datasets. Annual precipitation was derived from ERA5 daily precipitation.

To further evaluate the robustness of S_R estimate, we employed multiple independent datasets, including PML-V2 [30] and FLUXCOM evaporation products, Catchment Attributes, and MEteorology for Large-sample Studies (CAMELS) dataset [31], and the long-term total water storage (TWS). PML-V2, derived from the Penman-Monteith-Leuning (PML) model, incorporated stomatal conductance theory to couple the gross primary production (GPP) process. Given the intrinsic trade-off between GPP and evaporation, PML-V2 provided more accurate evaporation products than previous models for 2001–2020, with 8-day temporal resolution and 500 m spatial resolution. FLUXCOM was produced based on

machine learning methods that integrated FLUXNET site-level observations, satellite remote sensing, and meteorological data. The dataset spanned 2001–2020, with monthly temporal resolution and 0.5° spatial resolution for 2001–2015, and 8-day temporal resolution and 0.083° spatial resolution for 2016–2020. Both PML-V2 and FLUXCOM were resampled to 0.5°, and downscaled to daily temporal resolution referring to ERA5 daily evaporation. The CAMELS dataset provided daily meteorological forcing (including precipitation and temperature) and discharge for 453 catchments across the USA from 1980 to 2014. The long-term TWS was reconstructed from Gravity Recovery and Climate Experiment (GRACE) by combining machine learning with time series decomposition and statistical decomposition techniques, covering the period 1982–2019, with monthly temporal resolution and 0.5° spatial resolution [32].

In this study, land cover types were defined using the MODIS Land Cover Type product (MCD12Q1) for 2020 at a spatial resolution of 500 m. The dataset was resampled to 0.5° using a majority algorithm, which determines the new value of the cell based on the most popular values in the filter window. Glacier outlines (excluding the ice sheets in Greenland and Antarctica) were available from Randolph Glacier Inventory 6.0, lake boundaries were sourced from HydroLAKES, and global irrigation areas were obtained from Global Map of Irrigation Areas version 5.

2.2. Mass curve technique (MCT)

The mass curve technique (MCT), a deficit-based approach, was adopted to estimate S_R [9,10,33,34]. The method relies on the water balance, where inflow (F_{in}) to the root zone comprises daily precipitation, snowmelt, and irrigation, while outflow (F_{out}) corresponds to daily evaporation. Daily temperature is used to determine whether precipitation falls as rainfall or snowfall. If the temperature is below 0 °C, precipitation is considered as snowfall, and its value of rainfall for that day is set to zero.

The estimation of S_R involved calculating the water deficit in the root zone when the outflow (daily evaporation) exceeded the inflow (the sum of daily precipitation, snowmelt, and irrigation). This deficit indicates that plants rely on the water stored in S_R to sustain their water use, such as transpiration. The calculation of the outflow and inflow water deficit for each day is performed as follows Eq. (2):

$$A_{t_n \to t_{n+1}} = \int_{t_n}^{t_{n+1}} F_{out} - F_{in} dt. \quad (2)$$

$A_{t_n \to t_{n+1}}$ is the water deficit on day t_{n+1}. The aggregate of water deficit in each day is the accumulative water demand Eq. (3):

$$D_{t_{n+1}} = \max\left(0, D_{t_n} + A_{t_n \to t_{n+1}}\right). \quad (3)$$

$D_{t_{n+1}}$ is the accumulative water deficit on day t_{n+1}. It should be noted that D never becomes negative, as it represents a continuous estimate of the root zone storage reservoir. Considering the difference of seasonality variations across different climates (e.g., the monsoon climate with a dry period mainly in winter, while the Mediterranean climate in summer), D does not get back up to zero and the deficit is carried over to the next year. In general, the inflow of the root zone exceeds the outflow for annual totals. Therefore, to exclude the influence of abnormal data, we removed grid cells where the average annual inflow was less than the outflow from 1971 to 2020. In very rare cases, such as in arid regions, D may also accumulate over more than one year and data were reset if the accumulation extended over two consecutive years. This is because short-term plants dominate these regions, rapidly growing with early spring rain and snowmelt, completing their life cycle before the dry season, and surviving in seed or underground dormancy. Even under multiannual droughts, vegetation in these regions does not endlessly expand root zones to adapt to climate variability.

Since the S_R reflects ecosystems' long-term response to climate [9], we defined S_R in a given year as the maximum of a number of years' D:

$$S_R = \max\left(D_{t_1}, D_{t_2}, \cdots, D_{t_{end}}\right). \quad (4)$$

Because earlier work has shown that globally ecosystems tune to a drought of once in about 10 years [9], we used the maximum D of the past ten years as the S_R. For example, the maximum D from 1973 to 1982 was referred to as the S_R of 1982. Here, we used data from 1971 to 1972 as a spin-up period to prevent abnormal initial conditions. The conceptual illustration of the algorithm and some examples at the grid cell scale for calculating S_R are shown in Figs. S2a and S3 (online).

2.3. Trend analysis

In this study, the temporal and spatial patterns of S_R across global vegetated lands were analyzed at different scales, including the global, grid cell, and regional scales. The global S_R trend was estimated using regression analysis, with area-weighted average S_R calculated to account for the unequal area of 0.5° grid cells across latitudes. To assess the significance of the temporal trend, the standard deviation of S_R was also computed. At the grid cell scale, S_R trends were also derived by regression analysis, and the proportions of land area exhibiting increasing or decreasing S_R were quantified based on area-weighted calculations. At the regional scale, we examined S_R trends across 12 land cover types (Fig. S4 online), including evergreen needleleaf forests, evergreen broadleaf forests, deciduous needleleaf forests, deciduous broadleaf forests, mixed forests, closed shrublands, open shrublands, woody savannas, savannas, grasslands, croplands, and barren. For each land cover type, the trend of area-weighted average S_R was estimated via regression analysis, and the standard deviation was calculated to evaluate the significance of the trend.

To further explore ecosystem adaptation strategies to climate change, we also analyzed the trends of LAI and AI via regression analysis at the global, grid cell, and regional scales from 1982 to 2020. The LAI data used in this study represented the average of three datasets (GIMMS LAI4g, GLOBMAP LAI, and GLASS LAI). Since GLASS LAI dataset was only available for 1982–2018, we estimated the average of three LAI datasets for 2019–2020 by constructing a regression model. This model was developed using 10% random samples of the average LAI values calculated from all three datasets (GIMMS LAI4g, GLOBMAP LAI, and GLASS LAI) and from two datasets available for the full period (GIMMS LAI4g and GLOBMAP LAI) during 1982–2018 (Fig. S5 online).

2.4. Attribution analysis

Based on the MCT method, S_R represents the maximum accumulation of water deficit in the root zone during drought periods and can be decomposed into two main components: drought duration and average daily water deficit during drought, where S_R is equal to the product of drought duration and average daily water deficit (Figs. S2 and S3 online). We defined drought duration as the days corresponding to the S_R accumulated period (Fig. S2b online); and the average daily water deficit was determined by calculating the average difference between outflow (daily evaporation) and inflow (daily precipitation, snowmelt, and irrigation) during the drought duration (Fig. S2b online).

In this study, we investigated the impact of two drivers on S_R from 1982 to 2020 at the global, grid cell, and regional scales, and these two drivers correspond one-to-one with S_R. Based on this decomposition, if S_R increases, it must be caused by an increase in

drought duration, average daily water deficit, or both; and vice versa. We categorized the factors driving S_R changes into three main categories (Fig. S2b online): (1) If the direction of S_R trend is the same as the drought duration but opposite to the average daily water deficit, the S_R change is considered to be dominated by changes in drought duration. (2) If the direction of S_R trend is inverse to drought duration but the same as the average daily water deficit, the S_R change is considered to be dominated by changes in the average daily water deficit. (3) If the direction of S_R trend coincides with both drought duration and average daily water deficit, changes in both factors are considered to contribute to the change in S_R.

Using regression analysis, we assessed trends in drought duration and average daily water deficit at the global, grid cell, and regional scales, and determined the respective contributions of the two to the changes in S_R. The trends in drought duration and average daily water deficit were independent variables, enabling us to understand the relative importance of these two factors in driving the observed changes in S_R over time.

2.5. Uncertainty analysis

To further evaluate the robustness of S_R estimates, we employed two additional evaporation datasets and two independent approaches for validation. Firstly, PML-V2 and FLUXCOM from 2001 to 2020 were used as input evaporation at the grid cell scale to estimate S_R by the MCT method. The global average S_R trends derived from these datasets were then calculated by regression analysis.

Secondly, we applied the calibration of a hydrological model to streamflow observations to estimate root zone water storage capacity at the catchment scale. The FLEX hydrological model, which simulates catchment hydrological processes [35,36], was used in this study. The model has 10 free parameters that require calibration, including S_{umax}, which represents the root zone water storage capacity. The input data came from the CAMELS dataset [31]. To assess the temporal variation of the model parameters, we employed the Dynamic Identification Analysis method (DYNIA) [37]. In this study, we generated 40,000 sets of parameter combinations within the feasible range for 10 parameters, using a Monte Carlo framework and a Latin hypercube sampling technique. Each parameter set was associated with a streamflow simulation, for which a performance metric is calculated by the Kling-Gupta efficiency (KGE) with a five-year moving window [38]. We selected the optimal parameters with the highest KGE for each period and catchment, and then compared the trends between S_{umax} and S_R in 453 catchments. The distribution of the catchments is shown in Fig. S6 (online).

Thirdly, we used total water storage (TWS) variability, defined as the difference between the maximum and minimum TWS value in a year, as another validation for S_R. We calculated global average TWS variability from 1982 to 2019 through area-weighted calculation and analyzed the Spearman rank correlation between S_R and TWS variability. Glacier regions, lakes, and areas irrigated with groundwater over 80% were excluded from this analysis, since S_R mainly considers the change of subsurface water deficit.

3. Results

3.1. Increasing trend of global S_R with increasing drought duration

Over the past four decades, global evaporation has exhibited a predominantly increasing trend, while precipitation has decreased in the mid-to-low latitudes, snowmelt has declined in high-latitude regions, and irrigation has shown a slight overall increase (Fig. S7 online). These trends indicate a drying global climate, which in turn contributes to the increase in S_R. On a global scale, the average S_R increased from 182 mm to 202 mm from 1982 to 2020, with a trend of 0.56 mm a^{-1} ($P = 0.000$) and a standard deviation of 6.80 (Fig.1a). Multiplied by the terrestrial vegetation area (85 million km^2), the total increased volume of S_R over this period amounts to approximately 1652 billion m^3, equivalent to the total storage capacity of 42 Three Gorges reservoirs, the world's largest hydraulic engineering project. However, this overall trend was not consistent throughout the study period. Most of the increase in S_R took place 1991–2007, with a trend of 1.11 mm a^{-1} and a standard deviation of 5.37. In 1982–1990, S_R in fact slightly decreased, and in 2008–2020, S_R reached a plateau (Fig.1a).

Furthermore, we found a concurrent increasing trend in both S_R and AI (Fig. 1a; Fig. S8 online). To further explore how drought affects S_R, we decomposed S_R changes into contributions from drought duration (L in days) and average daily water deficit during drought ($\overline{WD}$ in mm d^{-1}) to determine whether S_R variation is primarily driven by the duration or intensity of drought (Fig. 1b). Overall, global S_R increase was significantly influenced by increasing drought duration (Fig. 1b). However, the contributions of drought duration and average daily water deficit varied across different periods, with average daily water deficit driving S_R changes in the first period (1982–1990) and drought duration playing a more prominent role in the recent period (1991–2020; Fig. 1b).

3.2. Spatial pattern of S_R variation and its drivers

The changes in S_R were spatially heterogeneous. At the grid cell scale, we observed increasing S_R trends in 65% of the global vegetated land (53%, $P < 0.1$; 12%, $P \geq 0.1$), and decreasing trends in 35% (24%, $P < 0.1$; 11%, $P \geq 0.1$; Fig. 2a; Fig. S9 online) over past four decades. Increasing trends were common in central USA, central Africa, northern Eurasia, and central South America, whereas decreasing trends were mostly found in dry regions of the western USA, southern Asia, northern China, southern Africa, and northeastern Australia.

We further examined the drivers of S_R change for each grid cell. Among regions with increasing S_R, 54% were associated with an increase of drought duration, 21% with a rise in average daily water deficit, and 25% with an increase of both (Fig. 2b). In regions with decreasing S_R, we found diminishing proportions of influence from drought duration, average daily water deficit, and the combined effect of both factors, accounting for 43%, 35%, and 22%, respectively (Fig. 2b). Overall, changes in drought duration played a dominant role in S_R dynamics.

Across 12 land cover types, we observed increasing S_R trends in 9 types and decreasing trends in 3 relatively dry types from 1982 to 2020 (Fig. 3). Increasing trends were found in forests, savannas, grasslands, and croplands, with the largest increase observed in deciduous broadleaf forests (1.10 mm a^{-1}, standard deviation: 14.32), followed by mixed forests (0.93 mm a^{-1}, standard deviation: 10.75). Decreasing trends were detected in shrublands and barren lands, with closed shrublands experiencing the largest decline (0.94 mm a^{-1}, standard deviation: 15.59). Further analysis of the drivers of S_R change revealed that increases in most land cover types were primarily associated with the increase in drought duration (Fig. S10 online). The decline in S_R for shrublands was mainly linked to a decrease in average daily water deficit, while in barren lands, reductions in both drought duration and average daily water deficit contributed to S_R decrease (Fig. S10 online).

3.3. Comparison between belowground S_R and aboveground greenness

To explore ecosystems' adaptation strategies to climate change, variations in belowground S_R were compared with aboveground

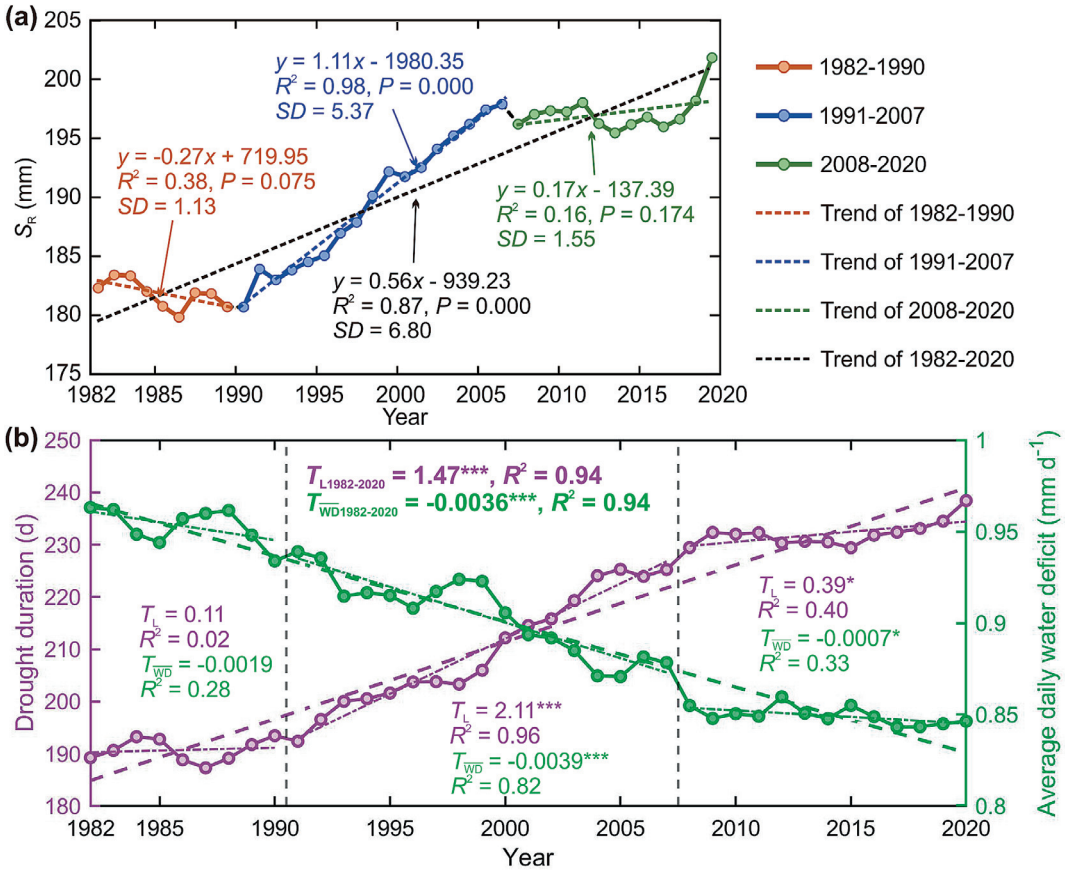

Fig. 1. Trends of global average S_R and its drivers. (a) Trends of global average S_R during the period 1982 to 2020. *SD* denotes the standard deviation. The dots represent the values of S_R for each year. (b) Trends of drought duration and average daily water deficit in global vegetated land from 1982 to 2020. The time is divided into three segments: 1982–1990, 1991–2007, and 2008–2020, corresponding to the divisions in Fig. 1a. The trend lines T_L and $T_{\overline{WD}}$ represent the changes in drought duration and average daily water deficit, respectively. To indicate the significance of the regression coefficients, the following symbols are used: * $P < 0.1$, ** $P < 0.01$, *** $P < 0.001$.

greenness (as represented by LAI), alongside changes in AI at both grid cell and regional scales. During 1982–2020, both S_R and LAI increased in a considerable fraction of global vegetated land (57%), while 8% showed S_R increases with LAI decreases, 4% exhibited concurrent declines, and 31% experienced S_R decreases with LAI increases (Fig. 4). Concurrent increases in S_R and LAI were predominantly found in central USA, the northern Amazon rainforest, eastern Europe, Siberia, eastern Asia, and the Congo rainforest, which were mostly in drying regions (Fig. S11 online). This suggested that vegetation in these areas was able to enhance S_R to adapt to increasing droughts while sustaining aboveground greening, supported by sufficient water availability. Concurrent S_R increase and LAI decrease were mainly concentrated in the boreal and tundra regions of northern North America and northern Asia, implying that the resilience of these ecosystems was threatened by climate drying. As drying intensified, these ecosystems required larger S_R to access more water to sustain basic physiological functions. But the limited water availability constrained their ability to sustain aboveground productivity increase. Areas with both S_R and LAI decreasing were distributed across the world, but were more common in arid regions. These ecosystems might already be transitioning or collapsing due to drought-driven stress. In response, they reduced both S_R and LAI as an adaptive strategy for survival, or in more extreme cases of water scarcity, this would manifest as degradation. Decreasing S_R trends that coincide with increasing LAI trends mainly appeared in regions of extreme humidity (such as northern South America and Malay Archipelago) and intensive human activities (such as western Europe, India). This might be explained by climate wetting (Fig. S11 online), shallow groundwater [39] and/or human-induced land cover change (such as agricultural expansion and/or intensification) [2,8,40].

As for different land cover types, S_R and LAI simultaneously increased in 9 out of 12 types in 1982–2020 (Fig. 3; Fig. S12 online), suggesting ecosystem in most types enhanced the root zone to adapt to intensified drought (Fig. S13 online). In contrast, three relatively dry types exhibited declining S_R despite increasing drought, while LAI continued to increase (Fig. 3; Figs. S12 and S13 online). This divergence may be explained by the positive effects of CO_2 fertilization and rising temperature, which potentially offset the negative impacts of decreased S_R on vegetation greenness. In particular, LAI increases in closed shrublands and barren lands were likely driven by CO_2 fertilization [7], whereas the greening in open shrublands was more associated with rising temperatures, which enhanced photosynthesis and led to longer growing seasons [7].

3.4. Validation of S_R trends using independent datasets and methods

To further validate our findings, we used multiple independent datasets and methods to verify the S_R trends at both global and catchment scales. At the global scale, PML-V2 and FLUXCOM global evaporation datasets were employed to estimate the S_R trend by MCT in 2010–2020, which are based on an energy-balance approach and an entirely data-driven algorithm, respectively. S_R estimates derived from PML-V2 closely aligned with those from ERA5 in magnitude, and both exhibited a similar increasing trend

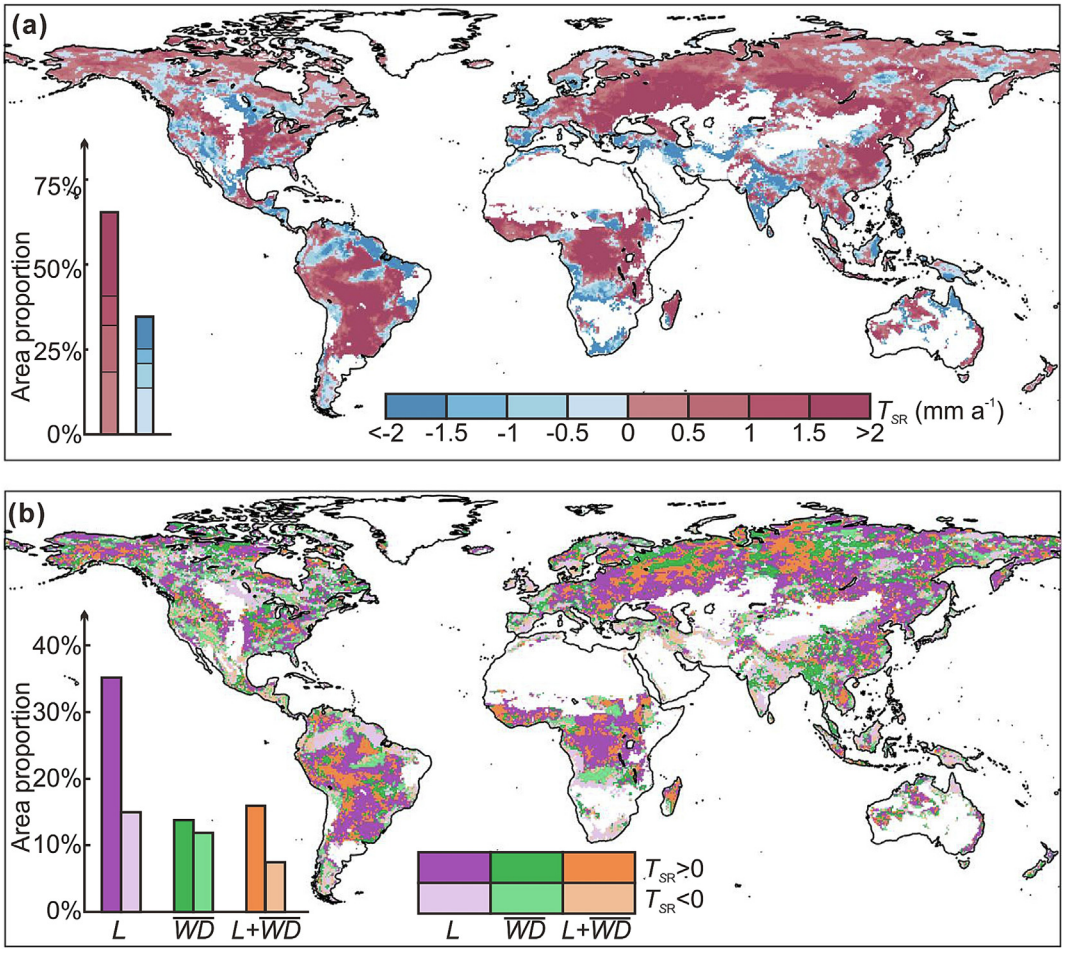

Fig. 2. Spatial pattern of S_R changes and its drivers. (a) Spatial distribution of the direction of S_R trends 1982–2020. T_{SR} denotes the trend of S_R. The histogram shows the percentage of areas with different S_R change types across global vegetated land (total 85 million km^2). (b) Dominant drivers affecting S_R change at grid cell scale. L, $\overline{WD}$, and $L+\overline{WD}$ denote drought duration, average daily water deficit, and both factors, respectively. The histogram shows the percentage of areas with different dominant factors for S_R changes across the global vegetated land.

to ERA5, with growth rates of 1.93 mm a^{-1} for PML-V2 and 1.57 mm a^{-1} for FLUXCOM (Fig. 5a), reinforcing the reliability of our estimate. Moreover, the global average S_R showed a positive rank correlation with intra-annual TWS variability from GRACE (r = 0.52, P = 0.001; Fig. S14 online) for 1982–2019. This provides another evidence showing the synchronicity between enhanced terrestrial total water deficit and increasing S_R, as the maximum deficit of root zone water storage.

At the catchment scale, long-term water balances also provided additional support for S_R increases under climate change. Using streamflow records from 453 CAMELS catchments across the USA from 1980 to 2014 [31], we calibrated the root zone water storage capacity parameter S_{umax} in a standard process-based hydrological model (FLEX) [35,36] via the Dynamic Identification Analysis (DYNIA) method [37,38]. Results showed that 86% (391 out of 453) catchments demonstrated an increasing trend of S_{umax} in 1980–2014, offering strong and independent evidence to support our main findings (Fig. 5b).

4. Discussion

This study showed a global increasing trend in S_R over the past four decades caused by increasing drought (primarily driven by drought duration, but also by the average daily water deficit during drought), as reflected in the aridity index (AI). Intensifying drought increases ecosystems' water demand; as a result, ecosystems allocate more carbon and nutrients to enhance their root zone systems [41], leading to an increase in S_R to sustain water supply. We found that global S_R slightly decreased from 1982 to 1990, then sharply increased until around 2007, after which it levelled off. Notably, S_R decreased abruptly in shrublands and barren lands (Fig. 3), while LAI showed a slight increasing trend (Fig. S12 online). However, the increase in aboveground biomass (LAI) does not indicate improved ecosystem resilience and may instead signal an expanding but more vulnerable ecosystem risk [42]. This potentially implies that ecosystems in these land cover types may have crossed ecosystems' thresholds or tipping points, which aligns with the breakpoints detected in global arid ecosystems using rain-use efficiency [43] and Normalized Difference Vegetation Index (NDVI) in remote sensing observations [44]. Additionally, the decreasing S_R in arid regions shortens the response time to drought [45], consistent with reports of degradation and regime shifts in arid grasslands, deserts, and drylands globally [43].

We found that most terrestrial ecosystems have tended to increase their S_R to adapt to intensifying droughts, while simultaneously sustaining Earth's greening over the past four decades. How ecosystems adapt or respond to changing climatic conditions is diverse. For instance, they may cope with increasing drought through aboveground greening due to CO_2 fertilization, or by increasing S_R, undergoing ecosystem transition (e.g., forest to savannah, or savannah to dry land) [46], or shifting in microbial

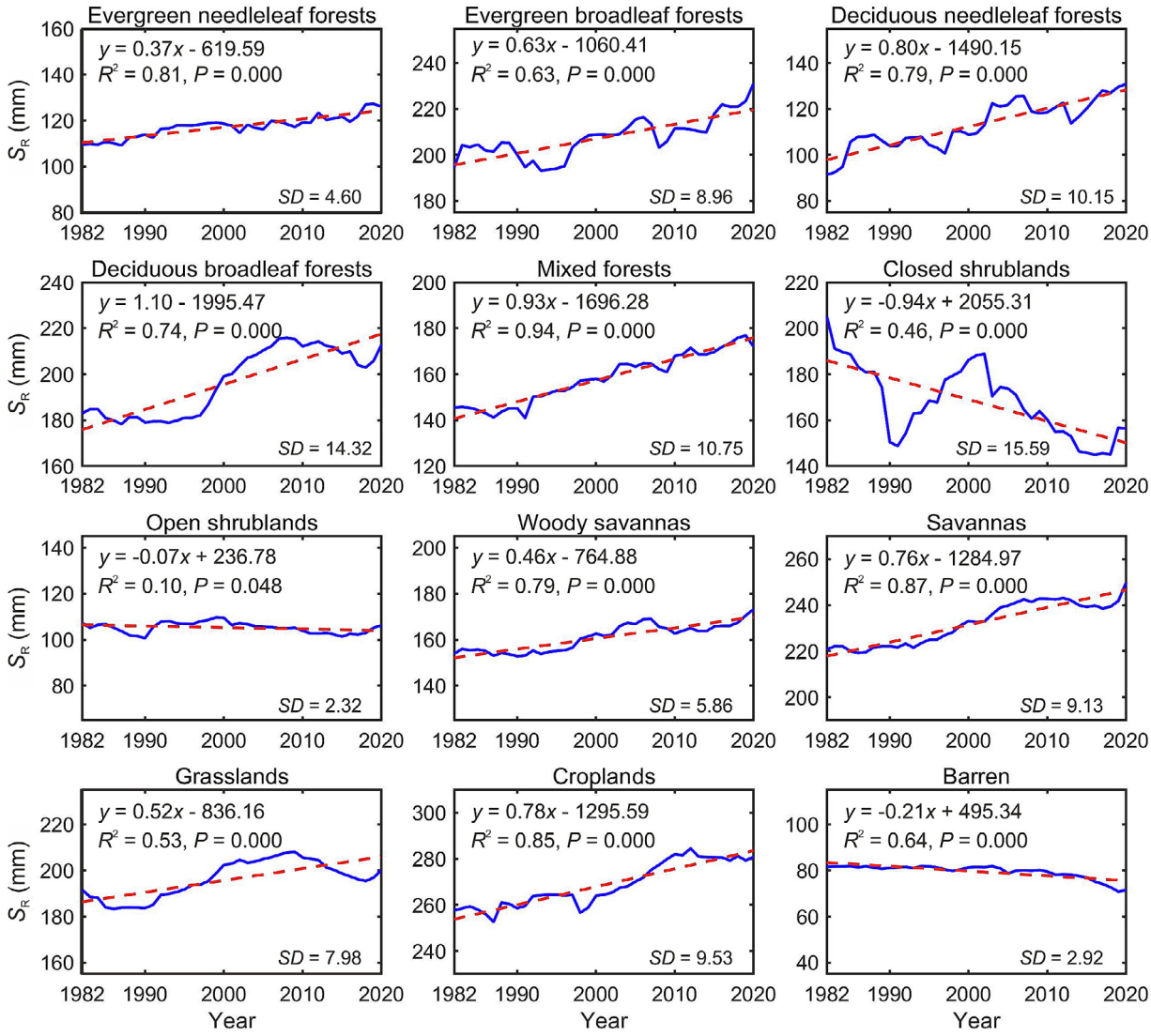

Fig. 3. Change of S_R in different land cover types in 1982–2020. *SD* denotes the standard deviation.

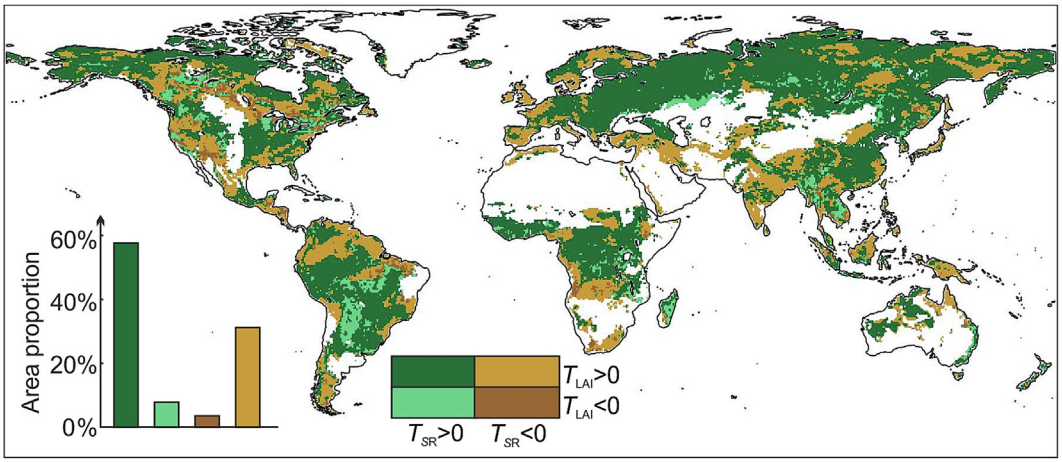

Fig. 4. The comparison between S_R and LAI from 1982 to 2020. The spatial pattern illustrates the areas with different colors for the four combinations of positive/negative T_{SR} (Trend of S_R) and T_{LAI} (Trend of LAI) in 1982–2020. The white regions represent areas with no vegetation cover and high uncertainty data. The accompanying histogram demonstrates the proportion of different combinations in the global vegetated area.

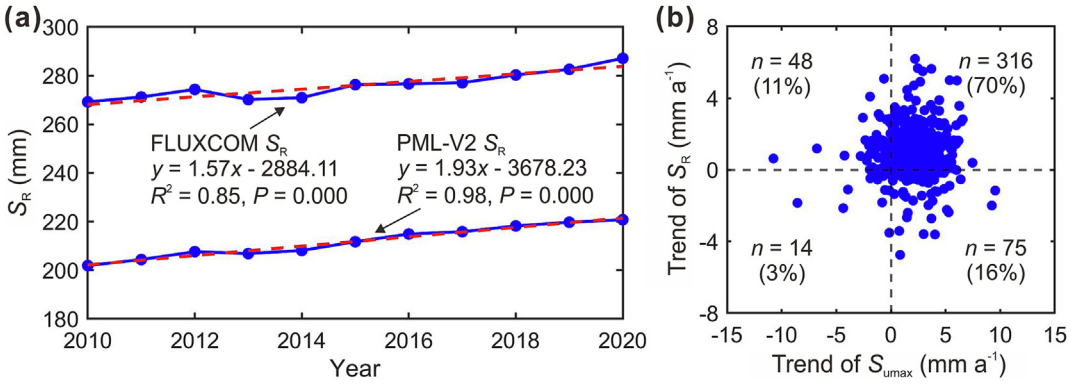

Fig. 5. More independent evidence supporting the increasing trend of root zone water storage capacity. (a) Trends of global average S_R estimated by PML-V2 and FLUXCOM for 2010–2020. (b) The scatter comparison of S_R and S_{umax} trend of 453 CAMELS catchments in the USA for 1980–2014. One dot represents one catchment.

communities [47]. Our finding implies that increasing S_R is likely one of the most effective and swift responses of ecosystems to intensifying drought. In regions with increasing S_R, ecosystems are still adapting to a changing climate. In regions with decreasing S_R, ecosystems may have reached the limit of their adaptive capacity. Neglecting S_R dynamics in climate impact assessments can, thus, lead to both under- and overestimations of climate risks to ecosystem health [46,48].

As an important part of the underground carbon pool, the root zone is critical for the global carbon budget. An enhanced root zone enables plants to access more water and nutrients, promoting the accumulation of both aboveground and belowground biomass and increasing organic matter input into the soil, ultimately enhancing the carbon sink. Based on the assumption of a proportional relationship between S_R and belowground biomass (Supplementary material and methods online), our study implicated a potential global increase in belowground biomass of 12.1 (9.6–14.4) GtC from 1982 to 2020. The largest increase might be occurred in evergreen broadleaf forests (3.9 GtC total, 3.5 tC ha^{-1}), potentially underscoring the importance of tropical ecosystems in the global carbon sink [49]; while the largest total reduction might be observed in open shrublands (−0.1 GtC), with the largest unit area reduction in closed shrublands (−2.1 tC ha^{-1}; Fig. S15 online). Although the assumption is reasonable, it does not consider the exponential decay of root biomass with depth and nutrient dynamics, which may introduce biases in belowground biomass estimates, particularly in water-unlimited regions. In this context, combining S_R with an asymptotic equation [50] may offer a useful approach for estimating fine root carbon. Nevertheless, further refinement and validation through controlled experiments or field studies are needed.

Globally, the increase in belowground root zone (11%; Fig.1a) slightly exceeded that of aboveground greening (10%; Fig. S16 online). Although plant biomass allocation among leaves, stems, and roots is commonly assumed to be a constant value [51], this assumption lacks rigorous testing. The root-leaf ratio is a vital expression to capture biomass allocation in plants, as both leaves and roots generally function as the resource-acquiring organs, in contrast to stems [52]. Our findings reveal that changes in roots and leaves–here loosely interpreted as trends in S_R and LAI, respectively–have the same direction in 61% of vegetated areas, but diverge in the remaining 39%. This suggests that plant biomass allocation does not remain fixed under climate change, challenging the common assumption of constancy.

In this study, S_R inferred by the climatological forcing reflects the ecosystems' actual response to climate change. It demonstrates that ecosystems enable to overcome the largest drought in the period of record. Similar to the storage capacity of an artificial reservoir, S_R represents the maximum storage capacity needed to ensure water supply during a critical drought, even though it is not fully utilized by ecosystems at all times. This redundancy is essential to guarantee water availability during droughts, with an acceptable probability of occurrence (i.e., the design return period). However, it is important to note that the climate-driven MCT method employed here is diagnostic rather than prognostic. As such, our findings describe historical ecosystem adjustments in S_R and should not be directly extrapolated to future conditions. In scenarios where drought will intensify and persist, further studies are needed to consider the full effects of climate change on vegetation physiology to project future S_R variation.

The ERA5 evaporation data employed in this study to derive S_R is expected to reproduce realistic evaporation dynamics, since the model-simulated evaporation from the land surface model HTESSEL [15,53] is adjusted based on assimilation using remotely sensed soil moisture and near-surface atmosphere conditions (e.g., air temperature and specific humidity) [54]. It has been shown that the assimilation procedure is able to correct evaporation for irrigation effects, even when irrigation is not applied in the land surface model [55]. Our results are further supported by the independent global evaporation datasets (PML-V2 and FLUXCOM; Fig. 5a), catchment-scale water balances (Fig. 5b), and intra-annual variations in TWS (Fig. S14 online). Moreover, a meta-analysis from field experiments across 110 published studies indicated that vegetation expands its root systems globally in response to the elevated concentration of CO_2 [56], corroborating our finding of global increases in S_R. The increasing trend of S_R is also consistent with globally drying trends of soil moisture [57], as vegetation water use reduces soil moisture and increases S_R.

Despite the use of state-of-the-art methods and datasets, and alignment with independent sources, the estimated S_R remains subject to uncertainties associated with forcing data quality. In particular, due to limited station density, ERA5 precipitation estimates are less accurate in desert regions [58], which have been excluded from this study. Snowmelt may be overestimated in high-latitude regions [59], but its impact is relatively minor compared to evaporation and precipitation. The irrigation data derived from four models (WaterGAP, H80, LPJmL, and PCR-GLOBWB) contain substantial uncertainties and are adjusted using correction factors to better align with reported data [26] to improve their accuracy.

This study primarily focuses on disentangling the effects of the proximate drivers, "drought duration" and "average daily water deficit during drought" on S_R changes. These drivers reflect the combined influences of natural fluctuations and human-induced changes in climate and land properties. While our analysis does not explicitly isolate the role of rising atmospheric CO_2, its effects are implicitly considered, as both vegetation and hydrological pro-

cesses respond to CO_2, temperature, and precipitation. Future studies should further differentiate the contributions of various drivers, including human activities and elevated CO_2 concentrations, to S_R variations. Additionally, the relationship between belowground S_R and aboveground greenness across different plant genera remains insufficiently understood and requires exploration using higher-resolution datasets. Although recent research has reported increased forest mortality under intensifying drought, such signals were not captured in this study, likely due to limitations in the spatial resolution (coarse 0.5° grid) and temporal scale (long-term trends exceeding ten years) [60]. These constraints may obscure short-term, localized variations in S_R and vegetation indices, highlighting the need for finer-scale observations in future assessments.

To the best of our knowledge, this is the first study to quantify the spatio-temporal variation of S_R at the global scale. We believe this study has improved our understanding of the mechanism of terrestrial ecosystems' resilience to drought and the role of belowground adaptation in maintaining the terrestrial biosphere within a safe operating space for humanity.

Conflict of interest

The authors declare that they have no conflict of interest.

Acknowledgments

This work was supported by the National Key Research and Development Program of China (2024YFF0809304), National Natural Science Foundation of China (42071081), the European Research Council (ERC-2016-ADG-743080, Horizon Europe 101081661), Formas (2022-02089 and 2019-01220), and the IKEA Foundation.

Author contributions

Qiaojuan Xi developed the method, performed analysis, drafted the manuscript, and reviewed and edited the manuscript. Hongkai Gao conceptualized the study, developed the method, assisted with the analysis, drafted the manuscript, and reviewed and edited the manuscript. Lan Wang-Erlandsson and Markus Hrachowitz developed the method, provided critical insights, and reviewed and edited the manuscript. Jianzhi Dong, Fabrizio Fenicia, and Hubert H. G. Savenije provided critical insights, reviewed, and edited the manuscript.

Data availability

The meteorological data used in this study were publicly available from the ERA5 reanalysis product (https://cds.climate.copernicus.eu/datasets/derived-era5-single-levels-daily-statistics?tab=overview). The irrigation data were sourced from the global gridded monthly sectoral water use dataset (https://zenodo.org/record/1209296#.Y2TrHWlByUk). For potential evaporation, we used data from the Global Land Evaporation Amsterdam Model (https://www.gleam.eu/). The LAI data were obtained from GIMMS LAI4g (https://zenodo.org/record/7649108), GLOBMAP LAI (https://zenodo.org/record/4700264#.Y_777D1ByUk), and GLASS LAI (http://www.glass.umd.edu/Download.html). To classify land cover types, we utilized data from MODIS Land Cover Type Product (MCD12Q1) (https://lpdaac.usgs.gov/products/mcd12q1v006/). PML-V2 evaporation data were produced by Zhang et al. (https://developers.google.com/earth-engine/datasets/catalog/CAS_IGSNRR_PML_V2_v018?hl=zh-cn). FLUXCOM energy fluxes data were accessible from the Data Portal of the Max Planck Institute for Biogeochemistry (https://www.bgc-jena.mpg.de/geodb/projects/Home.php). The hydrological model inputs were publicly available from CAMELS (https://doi.org/10.5065/D6MW2F4D). The long-term TWS data were reconstructed by Li et al. (https://datadryad.org/stash/dataset/doi:10.5061/dryad.z612jm6bt). The glacier outlines (excluding the ice sheets in Greenland and Antarctica) were available from Randolph Glacier Inventory 6.0 (https://nsidc.org/data/nsidc-0770/versions/6), the lake outlines were sourced from HydroLAKES (https://www.hydrosheds.org/products/hydrolakes), and the irrigation areas were obtained from Global Map of Irrigation Areas version 5 (https://www.fao.org/aquastat/zh/geospatial-information/global-maps-irrigated-areas/latest-version).

Appendix A. Supplementary material

Supplementary data to this article can be found online at https://doi.org/10.1016/j.scib.2025.06.027.

References

[1] Jackson RB, Mooney HA, Schulze ED. A global budget for fine root biomass, surface area, and nutrient contents. Proc Natl Acad Sci USA 1997;94:7362–6.
[2] Gherardi LA, Sala OE. Global patterns and climatic controls of belowground net carbon fixation. Proc Natl Acad Sci USA 2020;117:20038–43.
[3] Chandler MA. The Educational Global Climate Model (EdGCM). In our warming planet: topics in climate dynamics. In: Rosenzweig C, Rind D, Lacis A, Manley D, editors. Lectures in Climate Change. p. 411–28.
[4] Denissen JMC, Teuling AJ, Pitman AJ, et al. Widespread shift from ecosystem energy to water limitation with climate change. Nat Clim Chang 2022;12:677–84.
[5] Yuan W, Zheng Y, Piao S, et al. Increased atmospheric vapor pressure deficit reduces global vegetation growth. Sci Adv 2019;5:eaax1396.
[6] Yuan X, Wang Y, Ji P, et al. A global transition to flash droughts under climate change. Science 2023;380:187–91.
[7] Zhu Z, Piao S, Myneni RB, et al. Greening of the Earth and its drivers. Nat Clim Change 2016;6:791–5.
[8] Chen C, Park T, Wang X, et al. China and India lead in greening of the world through land-use management. Nat Sustain 2019;2:122–9.
[9] Gao H, Hrachowitz M, Schymanski SJ, et al. Climate controls how ecosystems size the root zone storage capacity at catchment scale. Geophys Res Lett 2014;41:7916–23.
[10] Wang-Erlandsson L, Bastiaanssen WGM, Gao H, et al. Global root zone storage capacity from satellite-based evaporation. Hydrol Earth Syst Sci 2016;20:1459–81.
[11] Zhu Y, Jia X, Qiao J, et al. Capacity and distribution of water stored in the vadose zone of the Chinese Loess Plateau. Vadose Zone J 2019;18:180203.
[12] McCormick EL, Dralle DN, Hahm WJ, et al. Widespread woody plant use of water stored in bedrock. Nature 2021;597:225–9.
[13] Bouaziz LJE, Aalbers EE, Weerts AH, et al. Ecosystem adaptation to climate change: the sensitivity of hydrological predictions to time-dynamic model parameters. Hydrol Earth Syst Sci 2022;26:1295–318.
[14] Mao G, Liu J. WAYS v1: a hydrological model for root zone water storage simulation on a global scale. Geosci Model Dev 2019;12:5267–89.
[15] Van Oorschot F, van der Ent RJ, Hrachowitz M, et al. Climate-controlled root zone parameters show potential to improve water flux simulations by land surface models. Earth Syst Dynam 2021;12:725–43.
[16] Kleidon A. Global datasets of rooting zone depth inferred from inverse methods. J Clim 2004;17:2714–22.
[17] Kleidon A, Heimann M. A method of determining rooting depth from a terrestrial biosphere model and its impacts on the global water and carbon cycle. Glob Chang Biol 1998;4:275–86.
[18] Schymanski SJ, Sivapalan M, Roderick ML, et al. An optimality-based model of the dynamic feedbacks between natural vegetation and the water balance. Water Resour Res 2009;45:W01412.
[19] Wang S, Hrachowitz M, Schoups G. Multi-decadal fluctuations in root zone storage capacity through vegetation adaptation to hydro-climatic variability has minor effects on the hydrological response in the Neckar basin, Germany. Hydrol Earth Syst Sci 2024;28:4011–33.
[20] Stocker BDD, Tumber-Davila SJ, Konings AGG, et al. Global patterns of water storage in the rooting zones of vegetation. Nat Geosci 2023;16:250–6.
[21] Nijzink R, Hutton C, Pechlivanidis I, et al. The evolution of root-zone moisture capacities after deforestation: a step towards hydrological predictions under change? Hydrol Earth Syst Sci 2016;20:4775–99.
[22] Schenk HJ, Jackson RB. ISLSCP II ecosystem rooting depths. In: ISLSCP Initiative II Collection. Oak Ridge, Tennessee, USA: ORNL DAAC; 2009. p. 1119–24.
[23] Fan Y, Miguez-Macho G, Jobbágy EG, et al. Hydrologic regulation of plant rooting depth. Proc Natl Acad Sci USA 2017;114:10572–7.

[24] Warren JM, Hanson PJ, Iversen CM, et al. Root structural and functional dynamics in terrestrial biosphere models-evaluation and recommendations. New Phytol 2015;205:59–78.
[25] Rippl W. The capacity of storage reservoirs for water supply. Minutes Proc Inst Civil Eng 1883;71.
[26] Huang Z, Hejazi M, Li X, et al. Reconstruction of global gridded monthly sectoral water withdrawals for 1971-2010 and analysis of their spatiotemporal patterns. Hydrol Earth Syst Sci 2018;22:2117–33.
[27] Cao S, Li M, Zhu Z, et al. Spatiotemporally consistent global dataset of the GIMMS leaf area index (GIMMS LAI4g) from 1982 to 2020. Earth Syst Sci Data 2023;15:4877–99.
[28] Liu Y, Liu R, Chen JM. Retrospective retrieval of long-term consistent global leaf area index (1981-2011) from combined AVHRR and MODIS data. J Geophys Res-Biogeo 2012;117:G04003.
[29] Xiao Z, Liang S, Wang J, et al. Long-time-series global land surface satellite leaf area index product derived from MODIS and AVHRR surface reflectance. IEEE Trans Geosci Remote Sens 2016;54:5301–18.
[30] Zhang Y, Kong D, Gan R, et al. Coupled estimation of 500 m and 8-day resolution global evapotranspiration and gross primary production in 2002-2017. Remote Sens Environ 2019;222:165–82.
[31] Addor N, Newman AJ, Mizukami N, et al. The CAMELS data set: catchment attributes and meteorology for large-sample studies. Hydrol Earth Syst Sci 2017;21:5293–313.
[32] Li F, Kusche J, Chao N, et al. Long-term (1979-present) total water storage anomalies over the global land derived by reconstructing grace data. Geophys Res Lett 2021;48:e2021GL093492.
[33] Grindley J. Calculated soil moisture deficits in the dry summer of 1959 and forecast dates of first appreciable runoff. Int Assoc Sci Hydrol 1960:109–20.
[34] Grindley J. The estimation of soil moisture deficits. Water for peace: water supply technology 1968:3–241.
[35] Fenicia F, Kavetski D, Savenije HHG. Elements of a flexible approach for conceptual hydrological modeling: 1. Motivation and theoretical development. Water Resour Res 2011;47:W11510.
[36] Fenicia F, McDonnell JJ, Savenije HHG. Learning from model improvement: on the contribution of complementary data to process understanding. Water Resour Res 2008;44:W06419.
[37] Wagener T, McIntyre N, Lees MJ, et al. Towards reduced uncertainty in conceptual rainfall-runoff modelling: dynamic identifiability analysis. Hydrol Process 2003;17:455–76.
[38] Liang J, Gao HK, Fenicia F, et al. Widespread increase of root zone storage capacity in the United States (preprint). EGUsphere 2024:1–29.
[39] Fan Y, Li H, Miguez-Macho G. Global patterns of groundwater table depth. Science 2013;339:940–3.
[40] Hauser E, Sullivan PL, Flores AN, et al. Global-scale shifts in rooting depths due to Anthropocene land cover changes pose unexamined consequences for critical zone functioning. Earth Future 2022;10:e2022EF002897.
[41] Arndal MF, Tolver A, Larsen KS, et al. Fine root growth and vertical distribution in response to elevated CO_2, warming and drought in a mixed heathland-grassland. Ecosystems 2018;21:15–30.
[42] Forzieri G, Dakos V, McDowell NG, et al. Emerging signals of declining forest resilience under climate change. Nature 2022;608:534–9.
[43] Bernardino PN, Keersmaecker WD, Fensholt R, et al. Global-scale characterization of turning points in arid and semiarid ecosystem functioning. Glob Ecol Biogeogr 2020;29:1230–45.
[44] Jiao W, Wang L, Smith WK, et al. Observed increasing water constraint on vegetation growth over the last three decades. Nat Commun 2021;12:3777.
[45] Vicente-Serrano SM, Gouveia C, Julio Camarero J, et al. Response of vegetation to drought time-scales across global land biomes. Proc Natl Acad Sci USA 2013;110:52–7.
[46] Singh C, Wang-Erlandsson L, Fetzer I, et al. Rootzone storage capacity reveals drought coping strategies along rainforest-savanna transitions. Environ Res Lett 2020;15:124021.
[47] Allsup CM, George I, Lankau RA. Shifting microbial communities can enhance tree tolerance to changing climates. Science 2023;380:835–40.
[48] Singh C, van der Ent R, Wang-Erlandsson L, et al. Hydroclimatic adaptation critical to the resilience of tropical forests. Glob Change Biol 2022;28:2930–9.
[49] Keenan TF, Prentice IC, Canadell JG, et al. Recent pause in the growth rate of atmospheric CO_2 due to enhanced terrestrial carbon uptake. Nat Commun 2016;7:13428.
[50] Jackson RB, Canadell J, Ehleringer JR, et al. A global analysis of root distributions for terrestrial biomes. Oecologia 1996;108:389–411.
[51] Ma H, Mo L, Crowther TW, et al. The global distribution and environmental drivers of aboveground versus belowground plant biomass. Nat Ecol Evol 2021;5:1110–22.
[52] Poorter H, Niklas KJ, Reich PB, et al. Biomass allocation to leaves, stems and roots: meta-analyses of interspecific variation and environmental control. New Phytol 2012;193:30–50.
[53] Balsamo G, Viterbo P, Beljaars A, et al. A revised hydrology for the ECMWF model: verification from field site to terrestrial water storage and impact in the integrated forecast system. J Hydrometeorol 2009;10:623–43.
[54] Hersbach H, Bell B, Berrisford P, et al. The ERA5 global reanalysis. Q J R Meteorol Soc 2020;146:1999–2049.
[55] Tuinenburg OA, de Vries JPR. Irrigation patterns resemble era-interim reanalysis soil moisture additions. Geophys Res Lett 2017;44:10341–8.
[56] Nie M, Lu M, Bell J, et al. Altered root traits due to elevated CO_2: a meta-analysis. Glob Ecol Biogeogr 2013;22:1095–105.
[57] Deng Y, Wang S, Bai X, et al. Variation trend of global soil moisture and its cause analysis. Ecol Indic 2020;110:105939.
[58] Liu R, Zhang X, Wang W, et al. Global-scale ERA5 product precipitation and temperature evaluation. Ecol Indic 2024;166:112481.
[59] Kouki K, Luojus K, Riihela A. Evaluation of snow cover properties in ERA5 and ERA5-Land with several satellite-based datasets in the Northern Hemisphere in spring 1982-2018. Cryosphere 2023;17:5007–26.
[60] Yan Y, Piao S, Hammond WM, et al. Climate-induced tree-mortality pulses are obscured by broad-scale and long-term greening. Nat Ecol Evol 2024;8:912–23.